ORIGINAL ARTICLE

A 3D turning surface model under the action of coupling dynamics of aerostatic spindle and cutting system

Dongju Chen[1] · Shupei Li[1] · Jinwei Fan[1]

Abstract

In this paper, a 3D surface topography model for ultra-precision turning is proposed, in which the coupling effect of turning dynamics and dynamics of the aerostatic spindle in microscale is considered. Firstly, the identification model of the tool-workpiece interference area is established by the analytical method, and then the accurate process damping coefficient is obtained. Meanwhile, considering the influence of the dynamic characteristics of the aerostatic spindle on the formation of the workpiece surface morphology, a 5-DOF aerostatic spindle dynamic model is established under the influence of the process damping effect in the cutting process and the microscale effect of the gas film. Then, based on the dynamic model of turning and aerostatic spindle, the surface topography model of ultra-precision turning is established. The effects of spindle speed, cutting width, and feed rate on the surface topography of ultra-precision turning are also analyzed. Finally, the cutting experiment is carried out, the surface morphology obtained from the simulation and experiment is characterized by three-dimensional surface roughness parameters, and the error between the simulation and experimental results is analyzed. The results show that the 3D surface morphology model built in this paper matches the experimental results better, which proves the effectiveness of the model.

Keywords Ultra-precision turning · Surface morphology · Dynamics · Aerostatic spindle · Process damping

1 Introduction

Ultra-precision turning, as one of the most widely used machining methods, has the advantages of high precision, strong machining ability of complex surfaces, and high machining efficiency, especially for the processing of complex optical components [1]. The surface topography of ultra-precision turning parts has a very important impact on its performance. The surface topography directly reflects the surface quality of parts, and the performance of parts can be indirectly evaluated by the surface topography of parts [2]. Ultra-precision turning is the result of the collaborative operation of many parts, and the error of any part will be more or less reflected on the machined parts. However, the most significant influence on the surface morphology of the workpiece is the spindle system and the cutting system composed of tool and workpiece. The dynamic behavior of them will have a very significant impact on the surface morphology of ultra-precision parts. Therefore, it is of great significance to establish a more accurate surface topography model for improving the machining quality of ultra-precision machining.

During the cutting process, due to the elastic recovery of the workpiece surface and the existence of vibration ripples, the tool flank will interfere with the machined surface of the workpiece. The direction of the ploughing force generated by this interference is opposite to the relative vibration direction between the tool and the workpiece, which in turn inhibits the relative vibration between the tool and the workpiece, and the effect is particularly significant in the low-speed machining process. The phenomenon that the cutting system spontaneously suppresses vibration, which occurs when the tool and the workpiece come into contact until the tool and the workpiece disengage and disappear, is called process damping. The process damping effect was first proposed by Sisson [3]. By studying the force acting on the tool directly behind the cutting edge, it provided a physical explanation for the low-speed cutting stability in accordance with the

✉ Dongju Chen
  djchen@bjut.edu.cn

[1] Mechanical Industry Key Laboratory of Heavy Machine Tool Digital Design and Testing, Faculty of Materials and Manufacturing, Beijing University of Technology, Beijing 100124, China

experimental results. Huang and Wang [4] systematically studied the influence of cutting conditions on the process damping, and the results showed that the process damping increased with the increase of feed rate, axial, and radial cutting depth, but decreased with the increase of cutting speed. Lee et al. [5] proposed a new mechanism model to study the nonlinear process damping force. The model uses a feedforward neural network to model the cutting force components and calculates the volume of the working material moved by the tool side to estimate the tool side and the process damping force generated by the interface between the machined surfaces. Budak and Tunc [6] proposed a method to identify process damping directly from flutter tests based on experimental and analytical stability limits. Budak and Tunc [7] further studied the damping identification method of the milling process. The process damping coefficients in the *x* and *y* directions were determined through the experimental stability limit, and the indentation coefficient was identified through the energy balance formula. Tyler and Schmitz [8] described an analytical solution for turning and milling stability including process damping effects and compared the new analytical solution, time-domain simulation, and experimental results. Cao et al. [9] proposed a semi-analytical method with high computational efficiency to calculate the interference volume between the honing tool and the workpiece during cutting. Turkes et al. [10] considered the two-degree-of-freedom complex dynamics model of the orthogonal cutting system turning and proposed a new process damping model and calculated the process damping ratio of low-speed cutting chatter during turning. However, the existing process damping identification models are solved by the discrete method, and the accuracy of the results is greatly affected by the discrete step size. Although a smaller step size can obtain good accuracy, it takes a lot of calculation time.

The cutting process is the result of the interaction between the tool and the workpiece. For ultra-precision turning, the cutting force received by the workpiece will be transferred to the aerostatic spindle equivalently. The main bearing medium of the aerostatic spindle is air, and the stiffness of the air film is far less than that of the workpiece, which means that in the ultra-precision turning process, the cutting force of the workpiece will be transferred to the aerostatic spindle equivalently. For the workpiece spindle system, the displacement of the spindle rotor is the main reason, which affects the surface topography of the workpiece. Therefore, it is necessary to study the dynamic characteristics of the spindle in the cutting process. Chen et al. [11] established the dynamic model of hydrostatic spindle motion error based on dynamic parameters, analyzed the variation law of spindle rotor motion error under unbalanced mass, and studied the characterization and evaluation technology of hydrostatic spindle rotation accuracy under unbalanced mass. Shi et al.

[12] established a 4-DOF radial gas bearing model and a 3-DOF thrust bearing model to model the whole gas spindle system and considered the influence of elastic deformation on the dynamic characteristics and tilt motion of the gas spindle. Chen and Chen [13] proposed a multi-field coupling five degrees of freedom dynamic model of aerostatic spindle considering the interaction of gas film, spindle, and motor. Chen et al. [14] established a dynamic model of the aerostatic spindle considering the microscale effect of film flow under the microscale condition and pointed out that when considering the microscale effect, the rotation error of the aerostatic spindle increases, and the response will be delayed. In addition, the clearance of aerostatic bearings is only a few to tens of microns, and the gas film will have a significant microscale effect when flowing in the microscale clearance, so the traditional Reynolds equation cannot describe the flow state of gas film in the microscale very well. Fukui and Kaneko [15] derived their FK model from a linearized Boltzmann equation. The basic equations are decomposed to describe the basic flow dependent on temperature, pressure, and velocity gradients. Considering the mass conservation, they incorporated these flows into the generalized Reynolds equation and analyzed the ultra-thin film lubrication. Based on the FK model and using mathematical technology, Yang and Shi [16] proposed a simplified Reynolds equation linearized flow rate (LFR) model to simulate ultra-thin film lubrication in a hard disk. The results show that the numerical results of the two models are in good agreement with each other and the relative error is small. The calculation efficiency of the simplified model is higher than that of the FK model. Zha et al. [17] introduced the LFR model into the study of the air film flow pattern of aerostatic bearing and verified the effectiveness of the LFR model in describing air film microscale flow pattern in aerostatic bearing clearance through theoretical and experimental verification.

However, the existing research on the dynamic characteristics of the aerostatic spindle system is based solely on the spindle itself, without considering the influence of the interaction between the tool and the workpiece on the dynamic characteristics of the spindle system under actual cutting conditions.

The cutting process is an extremely complex process. The main purpose of the cutting process is to obtain a high-quality machined surface. The surface topography determines the surface quality of the workpiece – different microscopic geometries of the surface of the workpiece. Usually, the inspection of the surface micro-topography requires cutting and then offline inspection, which is time-consuming and labor-intensive. Therefore, the establishment of an accurate mathematical model of the surface topography based on the interaction mechanism between the tool and the workpiece is of great significance for

improving the processing quality and reducing the cost of trial and error. Zhang et al. [18] established the surface topography model of the milling process by using discrete methods considering tool wear and proposed an algorithm for online simulation of surface topography. Shujuan et al. [19] proposed an improved Z-map algorithm to simulate the surface topography of parts machined by a ball-end milling cutter. Lu et al. [20] established the flexible deformation model of micro-milling cutter based on the instantaneous cutting thickness model, cutting force model, and dynamic characteristics of the micro-milling system. Based on the cutting tool path and the flexible deformation of the micro-milling cutter, a 3D surface topography simulation model is established. Lavernhe et al. [21] developed a 5-axis milling surface topography model based on the N-buffer method, which can be combined with a feed rate prediction model to provide guidance for using surface parameters to predict surface topography. Huang and Liang [22] established a surface topography model considering the cutting parameters of the tool and the relative vibration in the feed direction of the tool-workpiece, which can describe complex spherical and free-form surfaces. Lin and Chang [23] established a surface topography prediction model considering the relative motion of the tool and workpiece and the influence of tool geometry to simulate the surface finish profile of turning. Omar et al. [24] established a 3D milling surface topography prediction model considering the factors of tool runout, tool deflection, tool inclination, tool tooth wear, and system dynamics. He et al. [1] established a surface topography prediction model for single-point diamond turning considering the effects of kinematics, dynamics, and workpiece material defects and proposed a multi-frequency vibration model for the first time. Quinsat et al. [25] established a five-axis milling surface topography simulation model based on the N-buffer method and inverse kinematics transformation. Kelly et al. [26] studied the influence of machining dynamics on surface topography. The existing surface topography prediction model only considers the interaction between the tool and the workpiece and ignores the influence of the dynamic characteristics of the aerostatic spindle system on the surface topography of the workpiece.

In this paper, a 3D surface topography prediction model for ultra-precision turning processing is established, which takes into account the influence of the coupling effect of the cutting system and the spindle system on the surface topography. Firstly, a new analytical method for process damping in the cutting process is proposed, which realizes the precise identification of process damping. Based on the obtained cutting process damping, a dynamic model of the aerostatic spindle system under cutting conditions was established. Finally, considering the influence of the coupling dynamics of the cutting system and the spindle system, a prediction model for the surface morphology of ultra-precision turning is established, and the correctness of the model is verified through experiments.

2 Establishment of turning dynamic model

2.1 Effect of process damping

Process damping effect is an internal damping effect in the system caused by interference between tool flank and workpiece surface during the cutting process, which can significantly restrain chatter. Figure 1a shows an interference schematic between the cutter flank and the blunt circle of the cutter and the workpiece surface. Point A in Fig. 1 is the stagnation point; point F is the lowest point of the cutting edge; point O is the center of the tool blunt circle, and its radius is r; point E is the tangent point between the tool blunt circular arc and the straight section of the flank; point D is the intersection point between the tool flank and the boundary L. The interference section is shown in the area ACDEF in Fig. 1b.

According to reference [27], the process damping can be calculated according to Eq. (1):

$$C_{eq} = \frac{C_d K_y b}{v}; \quad C_d = \frac{\int_0^L S(x) \cos(\frac{2\pi}{L} x) dx}{Y \pi} \tag{1}$$

where C_d is the process damping coefficient; K_y is the cutting force coefficient; b is the cutting width; $S(x)$ is the interference

Fig. 1 (a) Interference pattern with blunt circular cutter and workpiece. (b) Diagram of tool and workpiece interference area
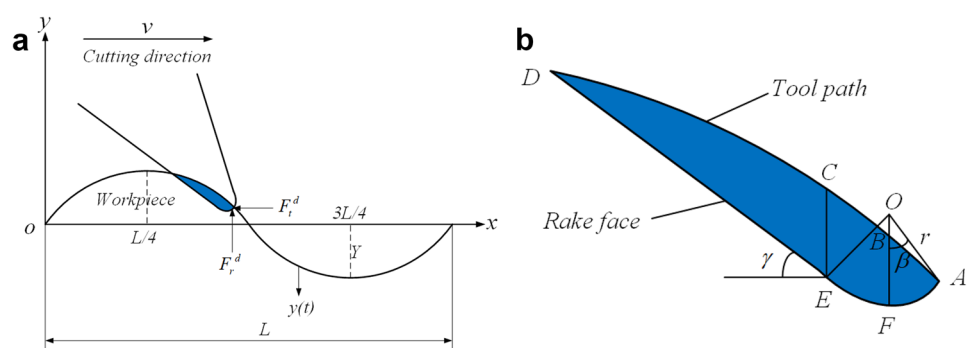
area of tool and workpiece; Y is the vibration amplitude; and L is vibration wavelength.

It can be seen from Eq. (1) that the key to solving process damping is to accurately calculate the interference area between tool and workpiece during cutting. Therefore, it is very important to accurately identify the interference area between the tool and workpiece for obtaining accurate process damping.

2.2 Interference area calculation

The existing research usually uses the discrete method to calculate the interference area between tool and workpiece, and the accuracy of the discrete method is closely related

$$S(x) = S_{ACEF}(x) + S_{CDE}(x) \tag{3}$$

Set the coordinate of stagnation point A to (x, y), then the coordinate of the blunt center O of the cutting edge is $(x - r\sin\beta, y + r\cos\beta)$. Thus, the equation of motion for any point (X, Y) on the blunt circle of the cutting edge can be written as follows:

$$(X - (x - r\sin\beta))^2 + (Y - (y + r\cos\beta))^2 = r^2 \tag{4}$$

From the geometric relationship in Fig. 1, the coordinate of point $E(x_E, y_E)$ can be determined as $(x - r\sin\beta - \sin\gamma, y - \cos\beta + \cos\gamma)$. Integrating from $x - r\sin\beta - \sin\gamma$ to x gets the area of area ACEF, as shown in Eq. (5):

$$S_{ACEF}(x) = \int_{x-r\sin\beta-\sin\gamma}^{x} \left[Y\sin(\lambda X) + \sqrt{r^2 - [X - (x - r\sin\beta)]^2} - Y\sin(\lambda x) - r\cos\beta \right] dX \tag{5}$$

to the selection of the discrete step. When the discrete step is long, the error of calculation results is large and the small discrete step will lead to time-consuming calculation. In this paper, the analytical method is used to build the tool-workpiece interference area model. This method is independent of the discrete step size and guarantees high accuracy without much time.

During ultra-precision turning, because the turning force is very small, the tool only vibrates in a small range under the action of cutting force. Therefore, it can be considered that the tool vibrates harmoniously, and the vibration displacement of the tool tip can be expressed by Eq. (2):

According to the coordinates of point E and the rake angle of the tool, the equation of the straight section of the tool in the two-dimensional orthogonal cutting model can be written, as shown in Eq. (6), where X_1 and Y_1 represent the coordinates of any point of the straight section of the tool flank and $k = \tan\gamma$ is the slope of the straight section.

$$Y_1 - (y - \cos\beta + \cos\gamma) = k\left[X_1 - (x - r\sin\beta - \sin\gamma)\right] \tag{6}$$

Simultaneous Eqs. (2) and (6) can obtain the intersection coordinate D of the straight section of the tool flank and the tool path. At this time, the area of the region CDE can be obtained by integrating the interval D-E, as shown in Eq. (7).

$$S_{CDE}(x) = \int_{x_D}^{x_E} \left[Y\sin(\lambda X_1) - \left(k - [X_1 - (x - r\sin\beta - \sin\gamma)] + y - \cos\beta + \cos\gamma\right) \right] dX_1 \tag{7}$$

$$y(x) = Y\sin(\lambda x); \ \lambda = \frac{2\pi}{L} \tag{2}$$

From Eqs. (5) and (7), the interference area at any place x can be obtained as follows:

$$
\begin{aligned}
S(x) &= S_{ACEF}(x) + S_{CDE}(x) \\
&= \int_{x-r\sin\beta-\sin\gamma}^{x} \left[Y\sin(\lambda X) + \sqrt{r^2 - [X - (x - r\sin\beta)]^2} - Y\sin(\lambda x) - r\cos\beta \right] dX \\
&+ \int_{x_D}^{x_E} \left[Y\sin(\lambda X_1) - \left(k - [X_1 - (x - r\sin\beta - \sin\gamma)] + y - \cos\beta + \cos\gamma\right) \right] dX_1
\end{aligned} \tag{8}
$$

As shown in Fig. 1b, the area ACDEF is divided into two parts, area S_{ACEF} and area S_{CDE}, using line segment CE:

The interference volume between tool and workpiece can be further calculated according to Eq. (9):

$$V(x) = b \cdot S(x) = b \cdot \left[S_{ACEF}(x) + S_{CDE}(x) \right]$$

$$= b \cdot \left[\begin{array}{l} \int_{x - r\sin\beta - \sin\gamma}^{x} \left[Y\sin(\lambda X) + \sqrt{r^2 - [X - (x - r\sin\beta)]^2} - Y\sin(\lambda x) - r\cos\beta \right] dX \\ + \int_{x_D}^{x_E} \left[Y\sin(\lambda X_1) - \left(k - \left[X_1 - (x - r\sin\beta - \sin\gamma) \right] + y - \cos\beta + \cos\gamma \right) \right] dX_1 \end{array} \right] \quad (9)$$

where b is the cutting width.

2.3 Establishment of the dynamic model

In the turning process, the y-direction, i.e., radial direction, has a great influence on the surface topography, which is the sensitive direction, while the other two directions have a less significant influence on the surface morphology. Therefore, a single-degree-of-freedom turning dynamic model in the y-direction shown in Fig. 2 is established in this paper. The expression is as follows:

$$M\ddot{y} + C\dot{y} + Ky = F(t) \quad (10)$$

where M is the modal mass; C is the model process, which can be obtained by $C = C_s + C_{eq}$. C_s is structure damping, and C_{eq} is process damping. K is the model stiffness; F is the cutting forces, and it can be determined by $F = K_f bh$; K_f is the cutting force coefficient.

3 Dynamic characteristics of aerostatic spindle

3.1 Microscale dynamic performance of the aerostatic spindle

The main bearing medium of the aerostatic spindle is air, which has significant compressibility compared with other kinds of media such as solids. Under the external load,
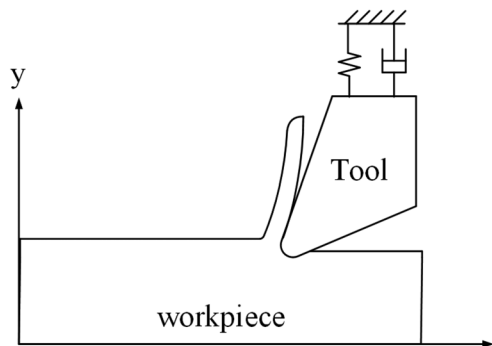
the gas film in the bearing clearance will be compressed, resulting in gas film fluctuation, affecting the distribution of gas film pressure in the bearing clearance and thus affecting the dynamic performance of the aerostatic spindle. However, the bearing clearance of aerostatic bearings is only a few microns, and the flow characteristics of gas in such a narrow bearing clearance are different from those of macro-scale. This microscale effect has a significant influence on the static and dynamic characteristics of aerostatic bearings. This paper uses the LFR model [16] to characterize the influence of the microscale effect on the gas film flow pattern. The LFR model is shown in Eq. (11):

$$\begin{cases} Q = C_1 + C_2/H \\ D = \dfrac{ph}{\mu\sqrt{2RT}} \end{cases} \quad (11)$$

where Q is the flow factor, which represents the microscale effect. D is the inverse Knudsen number. C_1 and C_2 are the coefficients related to D, and it can be determined as 0.99786 and 6.34676 by reference [17]. By introducing Eq. (11) into the traditional Reynolds equation and dimensionless calculation based on $x = \theta \cdot R$, $z = Z \cdot R$, $p = P \cdot p_a$, $\Omega = 12\mu R^2/(p_a h_o^2)$, $\Lambda = 6\mu UR/(p_a h_o^2)$, $h = H \cdot h_0$, a microscale gas film transient flow model can be obtained, as shown in Eq. (12):

$$\frac{\partial}{\partial\theta}\left((C_1 H + C_2) PH^2 \frac{\partial P}{\partial\theta} \right) + \frac{\partial}{\partial Z}\left((C_1 H + C_2) PH^2 \frac{\partial P}{\partial Z} \right) = \Lambda \cdot \frac{\partial(PH)}{\partial\theta} + \Omega \cdot \frac{\partial(PH)}{\partial t} \quad (12)$$

where R is the bearing radius; P_a is the atmospheric pressure; h_0 is bearing clearance thickness; p is the film pressure; h is the film thickness; μ is gas viscosity; U is the spindle speed; P and H are dimensionless gas film pressure and gas film thickness, respectively.

By using the perturbation method, the transient gas film pressure and the gas film thickness of the gas hydrostatic bearing in the microscale are obtained. Then, the transient film pressure is integrated along the surface, as shown in Eq. (13), and the dynamic stiffness and damping coefficient are obtained.

$$\begin{cases} K_n = \frac{\iint P_1 \cdot \cos\theta\, ds}{h} \\ K_t = \frac{\iint P_1 \cdot \sin\theta\, ds}{h} \end{cases} \qquad \begin{cases} C_n = \frac{\iint P_2 \cdot \cos\theta\, ds}{\omega h} \\ C_t = \frac{\iint P_2 \cdot \sin\theta\, ds}{\omega h} \end{cases} \quad (13)$$

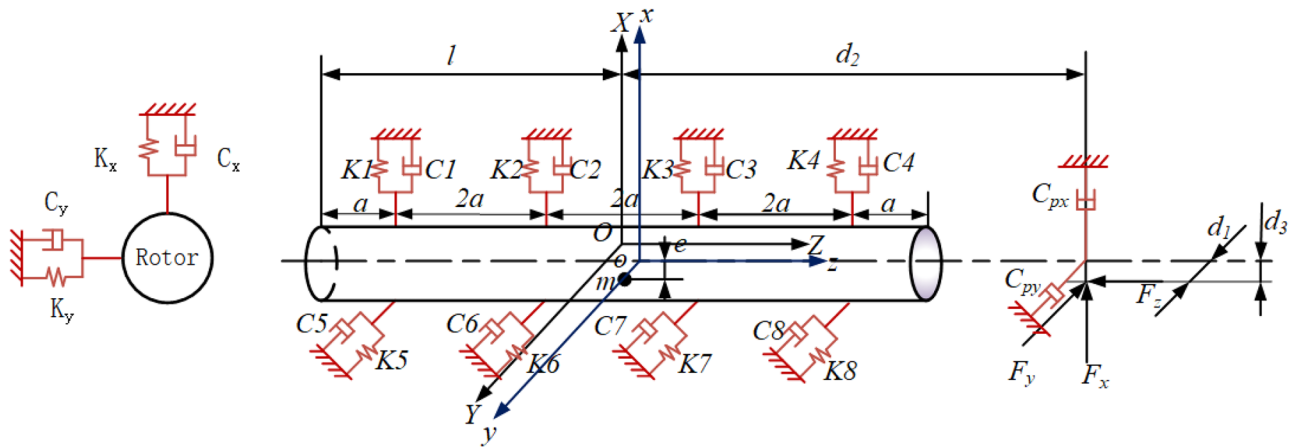**Fig. 2** Single-degree-of-freedom cutting model

Fig. 3 Dynamic model of aerostatic spindle system

where subscripts n and t indicate eccentric direction and perpendicular to eccentric direction, respectively. According to Eq. (13), the dynamic stiffness and damping at each orifice under different eccentricities are obtained, as shown in Eq. (14):

$$\begin{cases} K_i = K_n(\varepsilon_i), \ C_i = C_n(\varepsilon_i) \left(\varepsilon_i = x_i/h_0, i = 1 \sim 4\right) \\ K_i = K_t(\varepsilon_i), \ C_i = C_t(\varepsilon_i) \left(\varepsilon_i = x_i/h_0, i = 5 \sim 8\right) \end{cases} \quad (14)$$

3.2 Establishment of aerostatic spindle dynamic model

In the cutting process, interference between tool and workpiece can produce a process damping effect, which also affects the dynamic characteristics of the spindle. Therefore, a 5-DOF aerostatic spindle dynamic model considering

the damping effect of the cutting process is established, as shown in Fig. 3:

Figure 3 shows a schematic diagram of the dynamic model of the aerostatic spindle system. Since the orifice is the inlet to supply air pressure and has the highest pressure and bearing capacity at the orifice, so the orifice is simplified as a spring-damper system in this model. K_1-C_1, K_2-C_2, K_3-C_3, K_4-C_4 are the simplified stiffness-damping systems for orifices in the X-direction. K_5-C_5, K_6-C_6, K_7-C_7, K_8-C_8 are the simplified stiffness-damping systems for orifices in the Y-direction.

x, y, z are used to represent the displacement of the spindle along the X, Y, Z directions, and θ, ϕ, Ω respectively represent the angular displacement of the spindle around X, Y, Z. The aerostatic spindle dynamic model is established according to Newton's second law and Euler's angular momentum theorem, as shown in Eq. (15):

$$\begin{cases} m\ddot{x} + \left(\sum_{i=1}^{4} C_i \dot{x}_i + C_{px} \cdot \dot{x}_{px}\right) + \sum_{i=1}^{4} K_i x = me\omega^2 \cos\omega t + F_x + mg \\ m\ddot{y} + \left(\sum_{i=5}^{8} C_i \dot{x}_i + C_{py} \cdot \dot{x}_{py}\right) + \sum_{i=5}^{8} K_i y = me\omega^2 \sin\omega t + F_y \\ m\ddot{z} + C_z \dot{z} + K_z z = me\omega^2 \sin\sqrt{\theta^2 + \phi^2} + F_z \end{cases} \quad (15)$$

$$\Rightarrow \begin{cases} m\ddot{x} + (C_1 + C_2 + C_3 + C_4 + C_{px})\dot{x} + (K_1 + K_2 + K_3 + K_4)x \\ \quad = me\omega^2 \cos\omega t + F_x + mg - \left[a(3C_4 + C_3 - C_2 - 3C_1) + C_{px}d_2\right]\dot{\theta} \\ m\ddot{y} + (C_5 + C_6 + C_7 + C_8 + C_{py})\dot{y} + (K_5 + K_6 + K_7 + K_8)y \\ \quad = me\omega^2 \sin\omega t + F_y - \left[a(3C_8 + C_7 - C_6 - 3C_5) + C_{py}d_2\right]\dot{\phi} \\ m\ddot{z} + C_z \dot{z} + K_z z = me\omega^2 \sin\sqrt{\theta^2 + \phi^2} + F_z \end{cases}$$

$$
\begin{cases}
J_x\ddot{\theta} + \left(\sum_{i=5}^{8} C_i + C_{py}\right)\dot{\theta} + \left[9a^2(K_1 + K_4 + K_5 + K_8) + a^2(K_2 + K_3 + K_6 + K_7) + K_z R^2\right]\theta \\
= (J_y - J_z)w\dot{\phi} + (F_y d_2 + F_z\sqrt{d_1^2 - d_3^2})\cos\Omega + (F_x d_2 + F_z d_3)\sin\Omega - [F_x\sqrt{d_1^2 - d_3^2} + F_y d_3]\phi \\
J_y\ddot{\phi} + \left(\sum_{i=1}^{4} C_i + C_{px}\right)\dot{\phi} + \left[9a^2(K_1 + K_4 + K_5 + K_8) + a^2(K_2 + K_3 + K_6 + K_7) + K_z R^2\right]\phi \\
= (J_z - J_x)w\dot{\theta} - (F_y d_2 + F_z\sqrt{d_1^2 - d_3^2})\sin\Omega + (F_x d_2 + F_z d_3)\cos\Omega + [F_x\sqrt{d_1^2 - d_3^2} + F_y d_3]\theta
\end{cases}
\tag{16}
$$

Set up

$$
\begin{aligned}
&T = \sum_{i=1}^{4} C_i + C_{px}, T_1 = \sum_{i=5}^{8} C_i + C_{py} \\
&P = \sum_{i=1}^{4} K_i, P_1 = \sum_{i=5}^{8} K_i \\
&I = 3aC_4 + aC_3 - aC_2 - 3aC_1 + d_2 C_{px} \\
&I_1 = 3aC_8 + aC_7 - aC_6 - 3aC_5 + d_2 C_{py} \\
&S = 9a^2(K_1 + K_4 + K_5 + K_8) + (K_2 + K_3 + K_6 + K_7)a^2 + K_z R^2 \\
&S_1 = F_y d_2 + F_z\sqrt{d_1^2 - d_3^2} \\
&S_2 = F_x d_2 + F_z d_3 \\
&S_3 = F_x\sqrt{d_1^2 - d_3^2} + F_y d_3
\end{aligned}
\tag{17}
$$

Equation (18) can be obtained by sorting out Eqs. (15) and (16):

$$
\begin{aligned}
&\begin{bmatrix} m & & & & \\ & m & & & \\ & & m & & \\ & & & J_x & \\ & & & & J_y \end{bmatrix}
\begin{bmatrix} \ddot{x} \\ \ddot{y} \\ \ddot{z} \\ \ddot{\theta} \\ \ddot{\phi} \end{bmatrix}
+ \begin{bmatrix} T & 0 & 0 & I & 0 \\ 0 & T_1 & 0 & 0 & I_1 \\ 0 & 0 & C_z & 0 & 0 \\ 0 & 0 & 0 & T_1 & 0 \\ 0 & 0 & 0 & 0 & T \end{bmatrix}
\begin{bmatrix} \dot{x} \\ \dot{y} \\ \dot{z} \\ \dot{\theta} \\ \dot{\phi} \end{bmatrix}
+ \begin{bmatrix} P & 0 & 0 & 0 & 0 \\ 0 & P1 & 0 & 0 & 0 \\ 0 & 0 & Kz & 0 & 0 \\ 0 & 0 & 0 & S & S_3 \\ 0 & 0 & 0 & -S_3 & S \end{bmatrix}
\begin{bmatrix} x \\ y \\ z \\ \theta \\ \phi \end{bmatrix} \\
&= \begin{bmatrix} me\omega^2\cos\omega t + F_x + mg \\ me\omega^2\sin\omega t + F_y \\ me\omega^2\sin\sqrt{\theta^2 + \phi^2} + F_z \\ (J_y - J_z)w\dot{\phi} + S_1\cos\Omega + S_2\sin\Omega \\ (J_z - J_x)w\dot{\theta} - S_1\sin\Omega + S_2\cos\Omega \end{bmatrix}
\end{aligned}
\tag{18}
$$

Figure 4 shows the dynamic response of the translational displacement and angular displacement of the spindle system in the x and y directions. It can be seen from Fig. 4a–b that the process damping will significantly reduce the vibration amplitude of the spindle system in the x-direction and y-direction, accelerate the attenuation speed, and make the system reach the stable operation stage faster. Figure 4c–d shows that process damping can also reduce the irregular vibration of angular displacement at the initial stage of spindle operation.

It can be seen that the process damping effect will have a significant impact on the dynamic characteristics of the spindle system, which will further affect the generation of surface morphology in ultra-precision machining.

3.3 Simulation of dynamic characteristics of aerostatic spindle

Based on MATLAB 2018a and using the parameters shown in Table 1, the dynamic characteristics of the aerostatic spindle system under cutting conditions are simulated and analyzed.

4 Surface topography model of ultra-precision turning

4.1 Establishment of turning surface topography model

Cutting is the process of material removal by squeezing and friction between the tool and the workpiece. The tool profile

Table 1 Dynamics simulation parameters of aerostatic spindle

Parameter	Value
Spindle speed (r/m)	1000
Workpiece diameter (mm)	40
Cutting width (mm)	0.1
J_x (kgm^2)	0.7
J_y (kgm^2)	0.7
J_z (kgm^2)	0.026
e (μm)	0.5
d_1 (mm)	18
d_2 (mm)	200
d_3 (mm)	0.1

is reflected on the workpiece surface to form the machined surface. Since the tool is driven in the axial direction of the workpiece during turning, the path of any point on the tool on the workpiece is a helix, as shown in Fig. 5a. A plan

of the machined surface of the workpiece can be obtained by extending the workpiece along the bus bar, as shown in Fig. 5b.

For the workpiece surface spread diagram shown in Fig. 5b, the coordinates (z_k, y) of any point on the k-th tool path can be represented as

$$z_k = \frac{f}{Y} \cdot y + (k - 1) \cdot f \tag{19}$$

$$y(t) = 2\pi n \cdot R_0 \cdot t \tag{20}$$

where f is the feed per revolution; Y is the diameter of the workpiece; n is spindle speed; and R_0 is the radius of the workpiece.

The position of z_k at different processing times can be further determined by combining Eqs. (19) and (20).
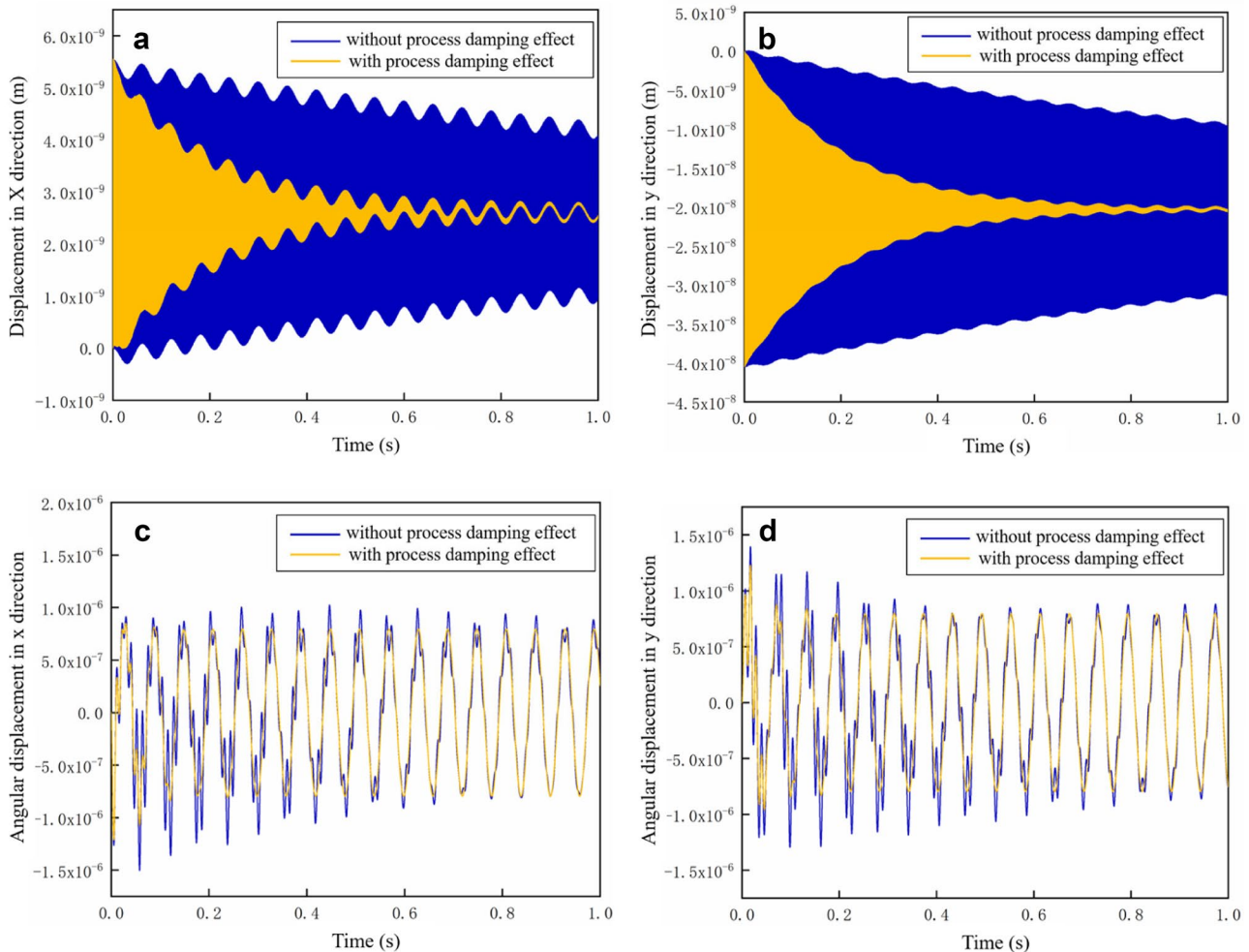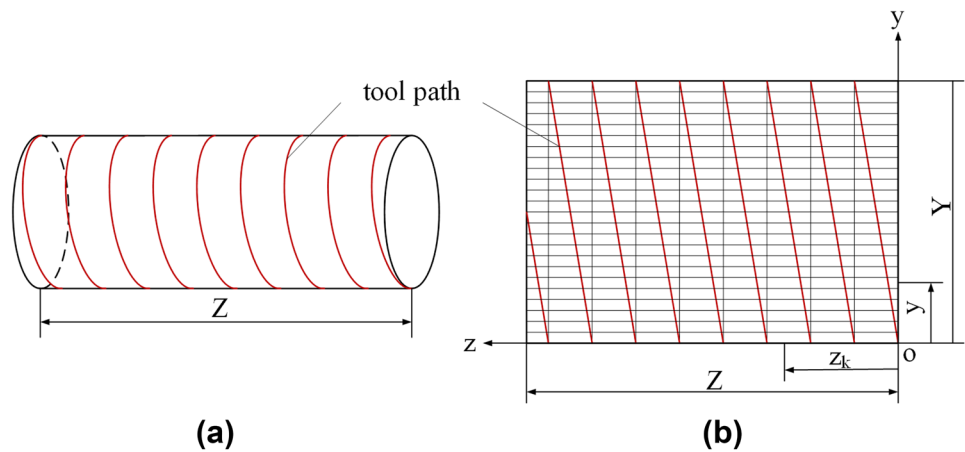
$$z_k(t) = n \cdot f \cdot t + (k - 1) \cdot f \tag{21}$$

Fig. 4 Simulation results of dynamic characteristics of aerostatic spindle: (**a**) displacement in x-direction; (**b**) displacement in y-direction; (**c**) angular displacement in x-direction; (**d**) angular displacement in y-direction

Fig. 5 (**a**) Profile of turning surface. (**b**) Workpiece surface deployment

(a)   **(b)**

The position of the point on the tool path at any time can be obtained from Eqs. (20) and (21).

In the cutting process, the residual traces of the tool on the workpiece surface constitute the surface morphology of the machined surface, as shown in Fig. 5. It can be seen from the figure that two adjacent tool paths will produce a coincidence area and a residual area. The coincidence area is the area where two tool paths are repeatedly removed, that is, the area above the dotted line in the figure. The residual area is the area below the solid line where both tool paths will not be removed. The fluctuation of this part constitutes the surface topography of the workpiece after machining. The fluctuation of this part of the region has a great relationship with the feed rate and the radius of the tool tip arc. According to the geometric relationship shown in Fig. 6, the expression of height h_k at any point on the tool path can be obtained as follows:

$$h_k = R_0 \cdot \left(1 - \sqrt{1 - \left(\frac{z - z_k}{R_0}\right)^2}\right) \tag{22}$$

It can be seen from Eq. (22) that the larger the radius of the tool tip arc or the smaller the feed rate will reduce the height of the intersection point of two adjacent tool paths, and the machined surface will be smoother and the surface quality will be better.

According to Eqs. (21) and (22), the position and height of any point on the surface of the workpiece shown in Fig. 5b can be obtained. But the result of Eq. (22) is an ideal state without vibration. In the actual machining process, the cutting system and spindle system inevitably generate vibration, which reflected on the surface of the workpiece will have a tremendous impact on the surface topography of the workpiece and form a new surface topography. In the process of ultra-precision turning, the main bearing medium of the aerostatic spindle, which is the key component of the machine tool, is gas, and its rigidity is much lower than that of the workpiece. Therefore, it is considered that during the turning process, only the spindle will generate vibration displacement under the action of cutting force. In addition, the tool will also produce vibration under the action of cutting force. Therefore, in the actual turning process, the vibration displacement which has the most significant impact on the surface morphology of the workpiece can be divided into two parts: the vibration of the aerostatic spindle and the vibration of the tool.

Figure 7 shows the effect of the relative vibration displacement between the tool and the workpiece on the surface topography. Figure 7a shows the effect of the vibration displacement along the radial direction of the workpiece on the surface morphology of the workpiece. It can be seen that the vibration displacement along the radial direction has a significant effect on the surface morphology of the workpiece,

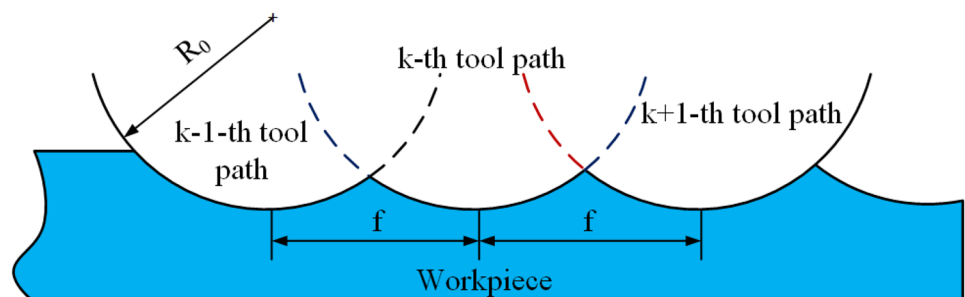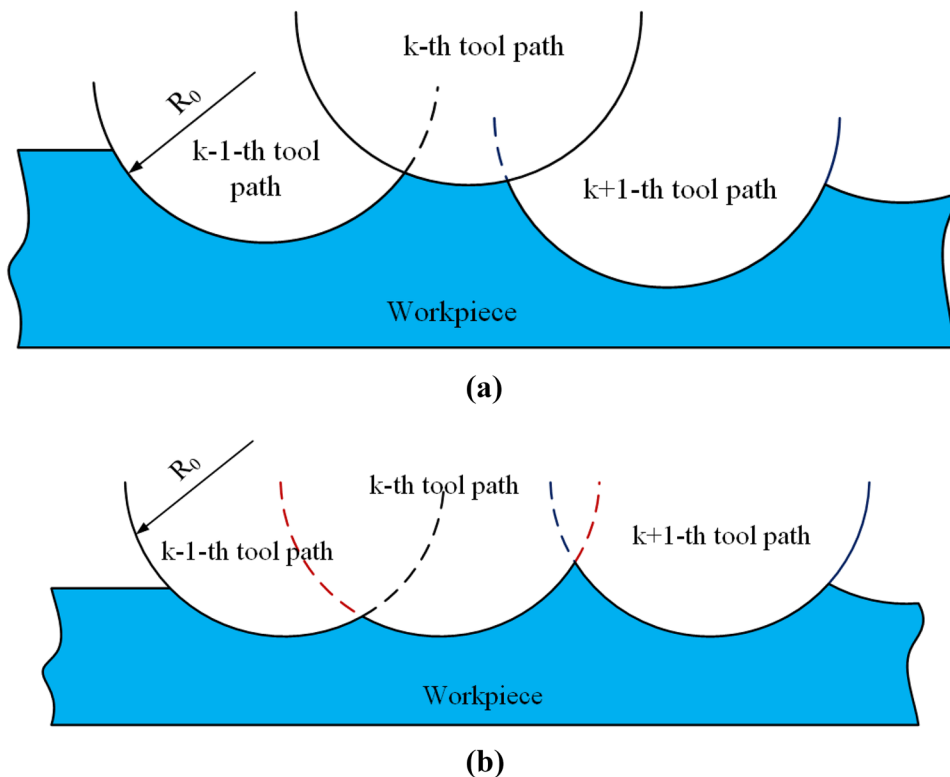**Fig. 6** Theoretical turning surface topography

Fig. 7 Effect of vibration displacement on the surface morphology of workpiece: (**a**) effect of vibration displacement in the radial direction; (**b**) effect of vibration displacement in the feed direction

(a)

(b)

especially the height between the wave crest and the wave trough. Figure 7b shows the effect of vibration displacement along the feed direction on the surface morphology of the workpiece. It can be seen that the vibration along the feed direction will have a certain impact on the peak value of the wave, but will not have an impact on the trough value, and its impact on the surface quality is smaller than that of the radial vibration.

By introducing the vibration displacement of the spindle and the vibration displacement of the tool into Eqs. (21) and

(22), the expression of the actual surface morphology of the workpiece on the grid point is obtained:

$$h_k = R_0 \cdot (1 - \sqrt{1 - (\frac{z - z_k}{R_0})^2}) + x_s(i,j) + x_t(i,j) \qquad (23)$$

$$z_k(t) = n \cdot f \cdot t + (k-1) \cdot f + z_s(i,j) \qquad (24)$$

where x, z is the vibration displacement in the x-direction and z-direction, respectively. The subscripts s and t denote the spindle and the tool, respectively.

4.2 Simulation of turning surface topography

Based on the established surface topography model, the dynamic displacement response caused by the nonlinear dynamic characteristics of the aerostatic spindle and the tool displacement response are introduced into the turning surface topography model. The parameters shown in the table below are used to simulate the surface morphology. The workpiece material is 7075 aluminum alloy with a diameter of 40 mm (Table 2).

Figure 8 shows the simulation results of turning surface topography with and without process damping effect at different spindle speeds. It can be seen from the figure that with the increase of spindle speed, although the surface morphology becomes more complex, the peak valley value shows a decreasing trend, which means that
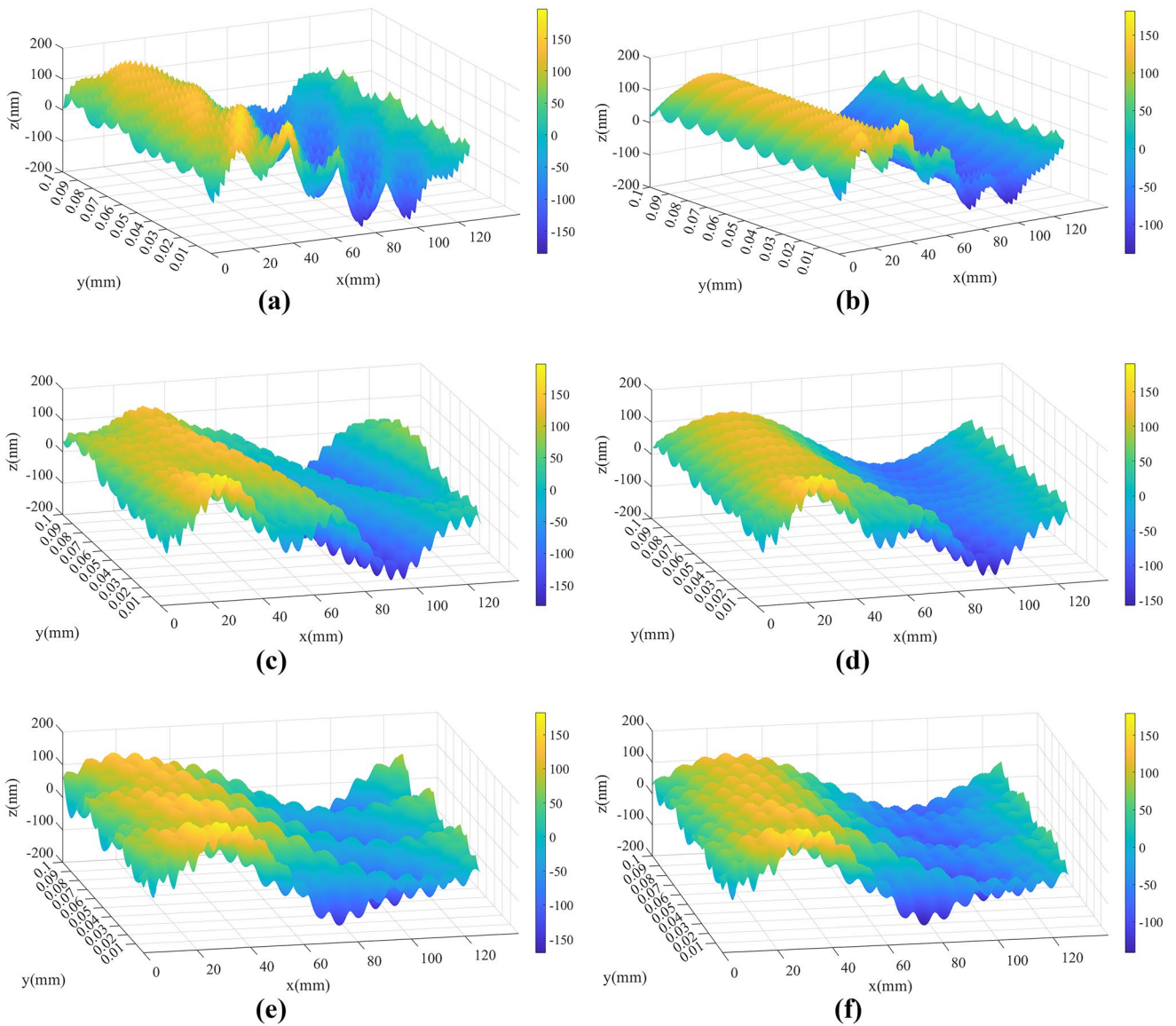
Table 2 Simulation parameters of ultra-precision turning surface morphology

Parameters	Value
Spindle speed n (rpm)	1000, 2000, 3000
Cutting width b (mm)	0.1, 0.2, 0.3
Feed rate f (mm/r)	0.01, 0.02, 0.03
K_y	10,000
Spindle mass m (kg)	2.6
Eccentricity e (μm)	0.5
a (mm)	13
M (kg)	0.58
C_s (Ns/m)	205
K (N/m)	6.39E7
K_f (Mpa)	1380
γ (°)	3
Tip radius r (mm)	0.5

Fig. 8 Effect of spindle speed on surface topography at $b=0.1$ mm, $f=0.01$ mm (**a**) $n=1000$ rpm without process damping; (**b**) $n=1000$ rpm with process damping; (**c**) $n=2000$ rpm without process damping; (**d**) $n=2000$ rpm with process damping; (**e**) $n=3000$ rpm without process damping; (**f**) $n=3000$ rpm with process damping

the surface quality actually becomes better. As can be seen in Fig. 8a, c, e and b, d, f, the surface morphology obtained by considering the process damping effect is more regular and the surface quality is relatively better than that obtained without considering the process damping effect. At the same time, it can be seen that the difference between the results of the two models decreases with the increase of spindle speed, which is caused by the weakening of process damping effect with the increase of spindle speed.

Figure 9 shows the simulation results of turning surface morphology with and without process damping effect under different cutting widths. It can be seen from the figure that with the increase of cutting width, the surface morphology fluctuates greatly along the circumferential direction. This means that the circumferential error of
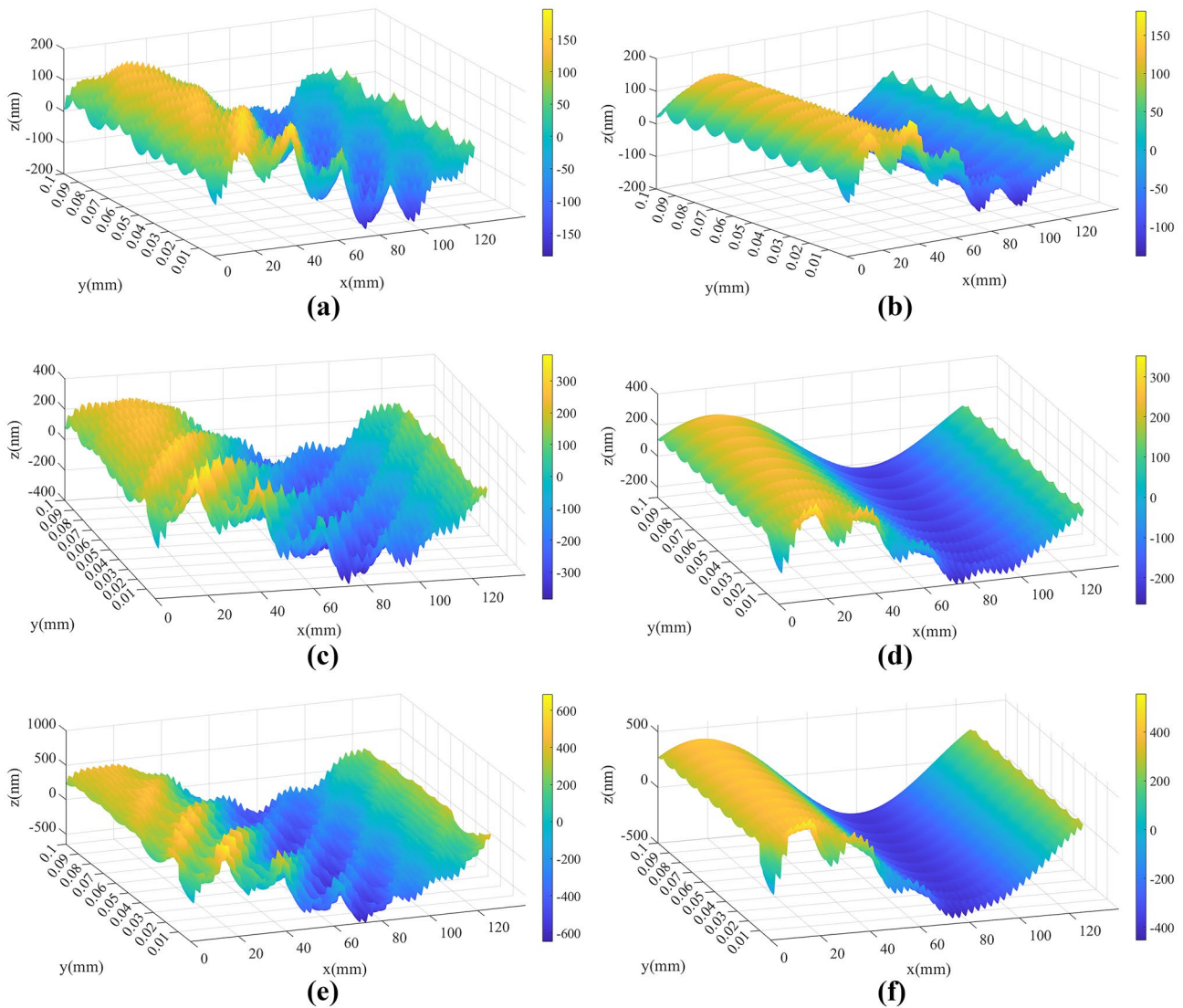
Fig. 9 Effect of turning width on surface morphology; $n=1000$ rpm, $f=0.01$ mm (**a**) $b=0.1$ mm without process damping; (**b**) $b=0.1$ mm with process damping; (**c**) $b=0.2$ mm without process damping; (**d**) $b=0.2$ mm with process damping; (**e**) $b=0.3$ without process damping; (**f**) $b=0.3$ with process damping

cutting increases and the cylindricity and concentricity of the workpiece decrease. The main reason is that with the increase of cutting width, the cutting force increases and the spindle vibration displacement caused by cutting force increases. Finally, the vibration displacement of the tool and the vibration displacement of the spindle are mapped to the workpiece surface, as shown in Fig. 9. Comparing Fig. 9a, c, e and b, d, f, it can be seen that the surface morphology obtained by considering the process damping

effect is more uniform and regular. And with the increase of cutting width, it can be seen that the uneven length at the initial stage of cutting decreases, because with the increase of cutting width, the process damping increases and the suppression of spindle vibration increases.

Figure 10 shows the simulation results of turning surface topography with and without process damping effect under different feed rates. It can be seen from the figure that the change of feed rate has no significant effect on the
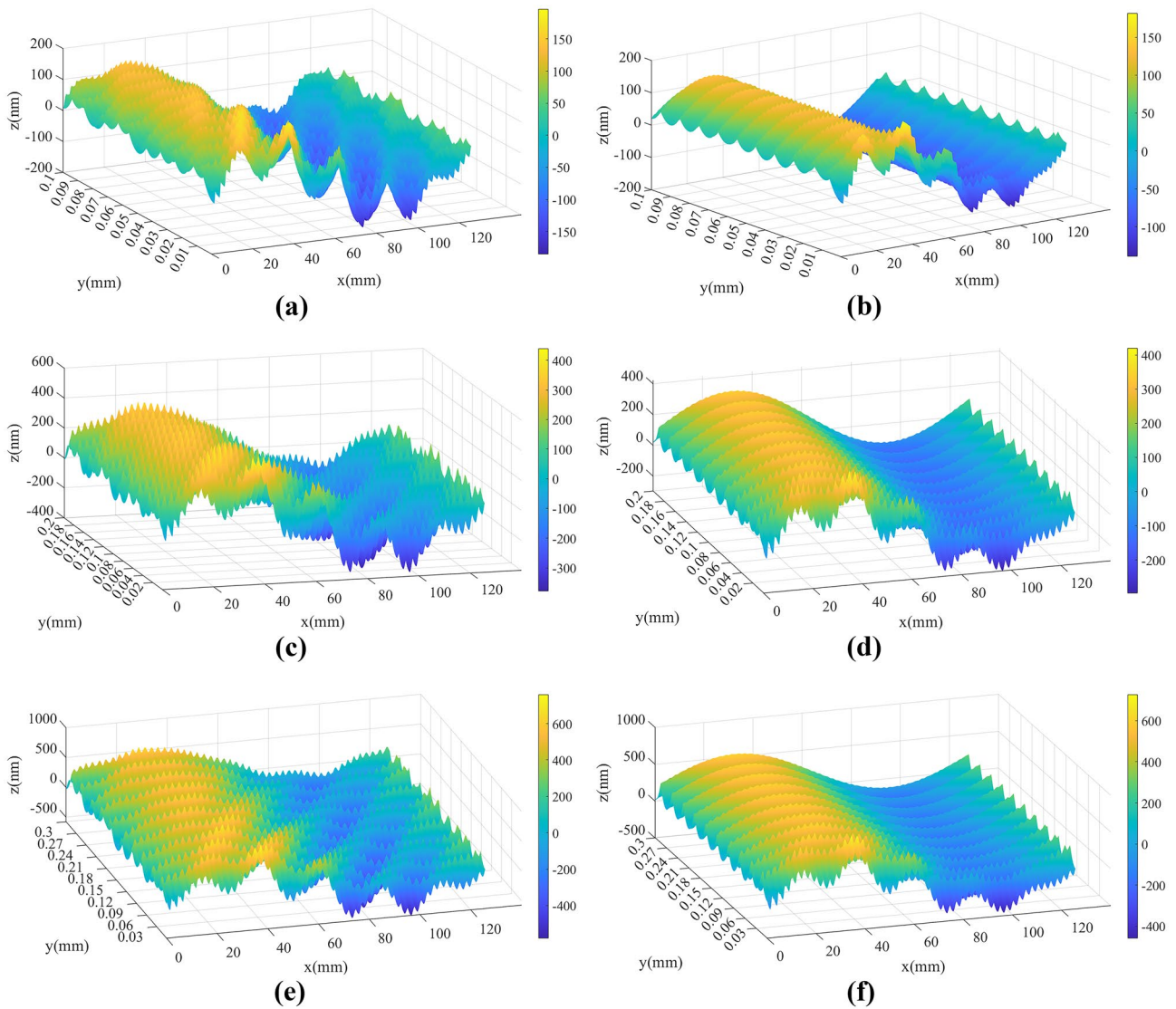
Fig. 10 Effect of feed rate on surface topography; $n=1000$ rpm, $b=0.1$ mm (**a**) $f=0.01$ mm without process damping; (**b**) $f=0.01$ mm with process damping; (**c**) $f=0.02$ mm without process damping; (**d**) $f=0.02$ mm with process damping; (**e**) $f=0.03$ mm without process damping; (**f**) $f=0.03$ mm with process damping;

distribution of surface morphology along the circumference and axis, but with the increase of feed rate, the peak and valley values of the surface increase significantly, which means that the surface quality tends to deteriorate. This is because with the increase of feed rate, the residual height left on the workpiece surface between adjacent tool paths increases, resulting in poor surface quality. Compared with Fig. 10a, c, e and b, d, f, it can be seen that the surface morphology obtained by considering the process

damping effect is more regular, and the strength of the process damping effect is not affected by the feed rate. In addition, the high-frequency vibration caused by the radial translation displacement of the spindle leads to the sawtooth distribution of the residual height of the workpiece surface, and the vibration displacement caused by the swing angular displacement of the spindle leads to the wavy distribution of the workpiece surface along the circumferential direction.
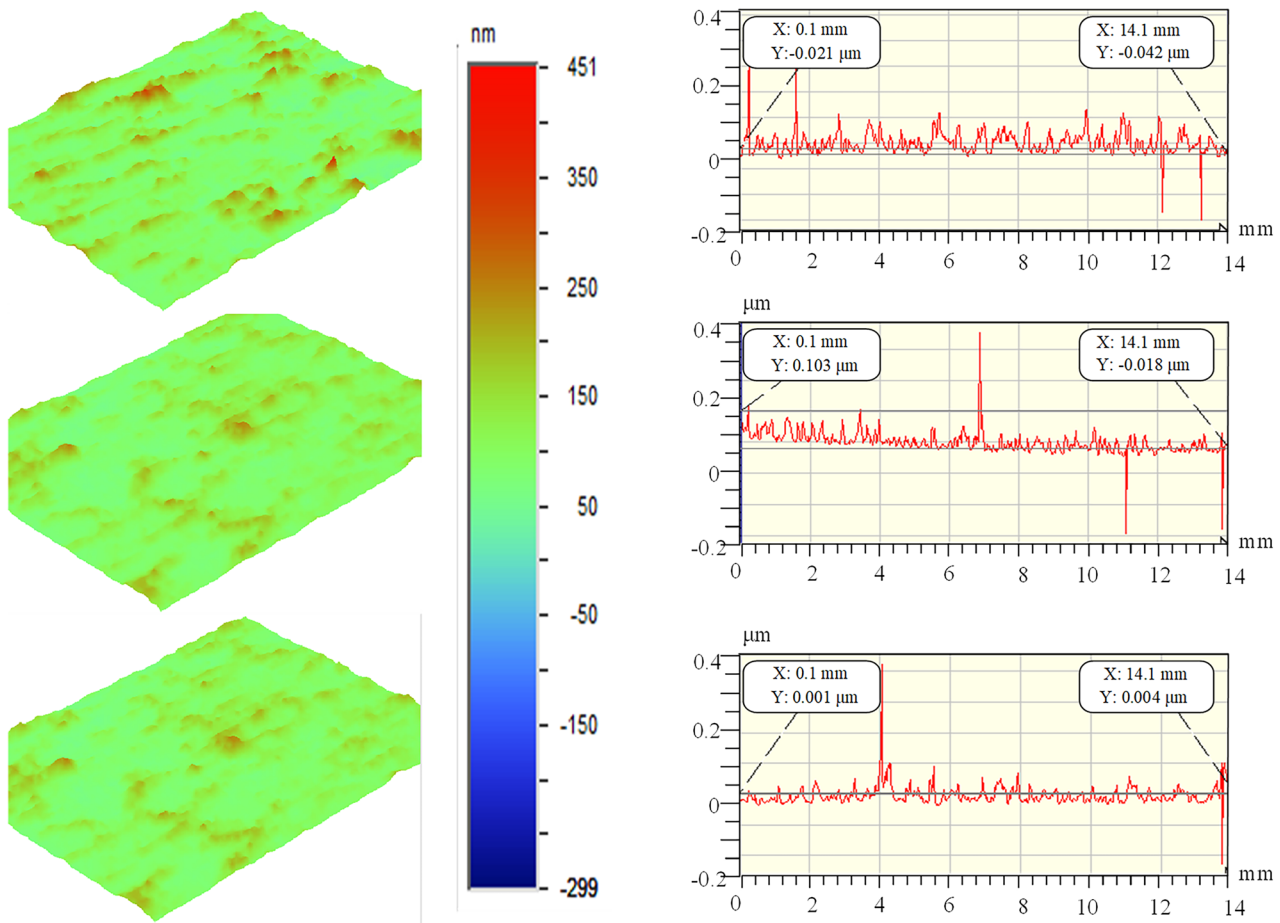
Fig. 11 Surface topography inspection results of ultra-precision turning aluminum alloy workpieces

4.3 Experimental verification

In order to verify the validity of the model, the aluminum alloy workpiece was cut on a single-point diamond lathe using simulation parameters. WYKO NT9300 optical profiler was used to detect the surface profile of the workpiece, the two-dimensional and three-dimensional topography of the detected surface was obtained, and the surface topography information was further obtained through data analysis.

Figure 11 shows the surface topography inspection results of the ultra-precision turning of aluminum alloy under the processing parameters of the spindle speed of 1000 r/min, the feed rate of 0.01 mm/r, and the cutting depth of 0.1 mm. During the measurement, three sets of data are measured along with different areas of the aluminum alloy processed surface in the circumferential direction.

In order to evaluate the surface topography more intuitively, three-dimensional surface roughness parameters, root

Table 3 Characterization parameters of workpiece surface morphology under different spindle speeds

| Spindle speed (r/min)	S_a (nm)			S_q (nm)			S_s (nm)		
	NPD	PD	EXP	NPD	PD	EXP	NPD	PD	EXP
1000	69.9398	66.3047	65.72	80.501	75.1472	76.88	382.1568	321.0029	361.25
2000	66.9172	62.6557	62.01	79.4514	72.3758	73.56	379.941	348.4297	358.53
3000	64.5167	60.2475	59.91	75.7223	69.7817	71.11	352.8767	320.8072	331.91
4000	55.4352	52.3876	53.25	66.859	62.4732	62.88	296.3845	291.1719	281.86
5000	45.7918	44.2173	44.97	55.2346	53.3707	51.96	251.1942	234.4175	218.02
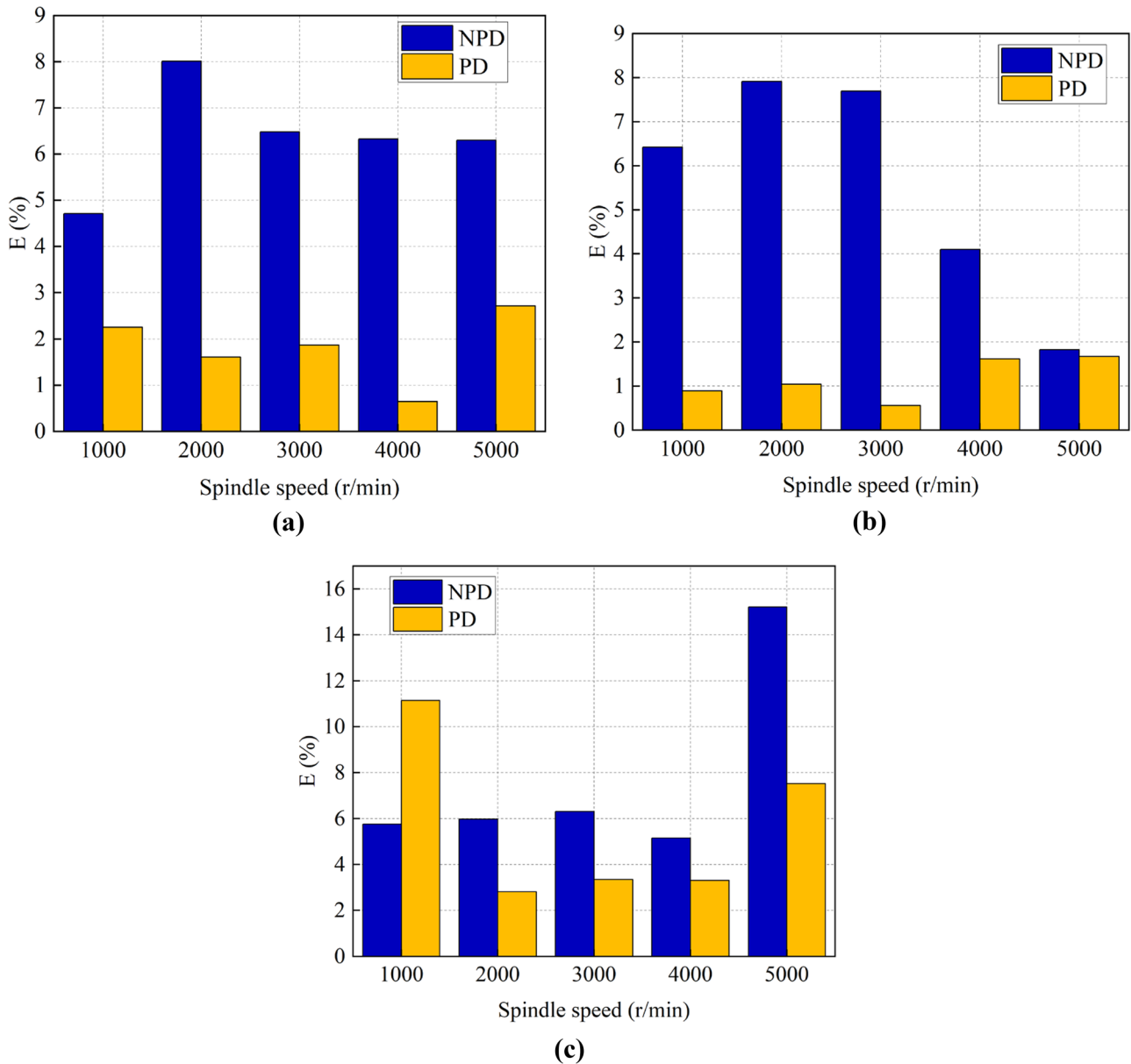
Fig. 12 Error comparison between simulation and experiment results: (**a**) prediction error of S_q; (**b**) prediction error of S_a; (**c**) prediction error of S_s

mean square deviation S_q, arithmetic average height S_a, and maximum height S_s are used to characterize the predicted and experimentally obtained surface topography.

The root mean square deviation S_q, the arithmetic average height S_a, and the maximum height S_s can be calculated by the following equations, respectively:

$$S_q = \sqrt{\frac{1}{A} \iint_A Z^2(x,y)\,dxdy} \tag{25}$$

$$S_a = \frac{1}{A} \iint_A |Z(x,y)|\,dxdy \tag{26}$$

$$S_s = \max_A Z(x,y) - \min_A Z(x,y) \tag{27}$$

The results of the root mean square deviation S_q, the arithmetic average height S_a, and the maximum height S_s of the surface topography obtained by simulation and experiment at different spindle speeds are shown in Table 3.

NPD represents the surface topography simulation result obtained without considering the process damping effect; PD represents the surface topography simulation result obtained by considering the process damping effect; EXP represents the surface topography result measured by the experiment.

In order to further quantitatively compare the degree of conformity between the surface topography model obtained by considering the process damping effect and the surface topography model obtained without considering the process damping effect and the surface topography obtained by the experiment, E is defined as the prediction error of the surface topography characterization parameter. The calculation equation is as follows:

$$E = \left| \frac{S_{i\text{measurement}} - S_{i\text{predict}}}{S_{i\text{measurement}}} \right| \times 100\% \tag{28}$$

Figure 12 shows the error between the surface topography characterization parameters obtained by the simulation with and without the process damping effect and the experimental results. It can be seen from the figure that the surface morphology established by considering the process damping effect is more consistent with the experimental results, and the error is smaller. This shows that the influence of the process damping effect on the surface quality of the workpiece cannot be ignored. The error comparison with the experimental results proves the correctness and accuracy of the surface topography prediction model built in this paper.

5 Conclusion

In this article, a new analytical method for process damping in the cutting process is firstly proposed. Then, considering the influence of cutting process damping and microscale effects, a dynamic model of the aerostatic spindle system is established. Finally, considering the influence of the coupling dynamics of the cutting system and the spindle system, a prediction model of the ultra-precision machining surface morphology was established and verified by experiments. The experimental results and error analysis show that the surface morphology prediction model established in this paper is highly consistent with the experimental results, which proves the effectiveness of the model established in this paper.

1. Spindle speed, cutting width, and feed rate have significant effects on surface morphology. With the increase of spindle speed, the surface morphology is more irregular, but the surface peak and valley value decreases; that is, the surface quality becomes better. With the increase of cutting width, the surface morphology becomes more complex, the peak valley value becomes larger and the surface quality becomes worse. At the same time, the fluctuation along the circumferential direction becomes larger, which means that the roundness of the workpiece surface becomes worse. With the increase of feed speed, although there is no significant difference in surface morphology along with the circumferential and axial directions, the peak valley value increases significantly. This is related to the increase of feed rate, resulting in the increase of residual height on the workpiece surface.

2. The process damping effect of the cutting system will significantly affect the dynamic characteristics of the spindle system, and the coupling dynamic characteristics of the cutting system and the spindle system will further significantly affect the generation of surface morphology in ultra-precision machining. Specifically, the surface morphology obtained by considering the process damping effect is more regular and has less fluctuation than that obtained without considering the process damping effect. However, the process damping effect will weaken with the increase of spindle speed, and the influence on the surface morphology will become smaller.

3. By comparing the errors between the surface topography model with and without process damping effect and the experimental results, it can be found that the surface topography prediction model with process damping effect is more consistent with the experimental results, which proves that the coupling dynamic characteristics of cutting system and spindle system have a significant impact on the surface topography of ultra-precision cutting. The correctness of the model is proven.

Declarations

References

1. He CL, Zong WJ, Xue CX, Sun T (2018) An accurate 3D surface topography model for single-point diamond turning. Int J Mach Tool Manuf 134:42–68

2. He C, Zong W (2019) Influencing factors and theoretical models for the surface topography in diamond turning process: a review. Micromach Basel 10(5):288

3. Sisson TR, Kegg RL (1969) An explanation of low-speed chatter effects 951–958

4. Huang CY, Wang JJJ (2007) Mechanistic modeling of process damping in peripheral milling 10–12

5. Lee BY, Tarng YS, Ma SC (1995) Modeling of the process damping force in chatter vibration. Int J Mach Tool Manuf 35(7):951–962

6. Budak E, Tunc LT (2009) A new method for identification and modeling of process damping in machining

7. Budak E, Tunc LT (2010) Identification and modeling of process damping in turning and milling using a new approach. CIRP Ann 59(1):403–408

8. Tyler CT, Schmitz TL (2013) Analytical process damping stability prediction. J Manuf Process 15(1):69–76

9. Cao C, Zhang XM, Huang T, Ding H (2020) An improved semi-analytical approach for modeling of process damping in orthogonal cutting considering cutting edge radius. Proc Inst Mech Eng B J Eng 234(3):641–653

10. Turkes E, Orak S, Neseli S, Yaldiz S (2011) A new process damping model for chatter vibration. Measurement 44(8):1342–1348

11. Chen D, Zhao Y, Liu J (2020) Characterization and evaluation of rotation accuracy of hydrostatic spindle under the influence of unbalance. Shock Vib

12. Shi J, Cao H, Maroju N K, Jin X (2020) Dynamic modeling of aerostatic spindle with shaft tilt deformation. J Manuf Sci E-T ASME 142(2)

13. Chen G, Chen Y (2021) Multi-field coupling dynamics modeling of aerostatic spindle. Micromach Basel 12(3):251

14. Chen D, Li N, Pan R, Han J (2019) Analysis of aerostatic spindle radial vibration error based on microscale nonlinear dynamic characteristics. J Vib Control 25(14):2043–2052

15. Fukui S, Kaneko R (1988) Analysis of ultra-thin gas film lubrication based on linearized Boltzmann equation: first report—derivation of a generalized lubrication equation including thermal creep flow 253–261

16. Shi BJ, Yang TY (2010) Simplified model of Reynolds equation with linearized flow rate for ultra-thin gas film lubrication in hard disk drives. Microsyst Technol 16(10):1727–1734

17. Zha C, Li T, Zhao Y, Chen D (2020) Influence of microscale effect on the radial rotation error of aerostatic spindle. Proc Inst Mech Eng J J Eng 234(7):1131–1142

18. Zhang C, Zhang H, Li Y, Zhou L (2015) Modeling and on-line simulation of surface topography considering tool wear in multi-axis milling process. Int J Adv Manuf Tech 77(1–4):735–749

19. Shujuan L, Dong Y, Li Y, Li P, Yang Z (2019) Geometrical simulation and analysis of ball-end milling surface topography. Int J Adv Manuf Tech 102(5):1885–1900

20. Lu X, Hu X, Jia Z, Liu M, Gao S, Qu C, Liang S (2018) Model for the prediction of 3D surface topography and surface roughness in micro-milling Inconel 718. Int J Adv Manuf Tech 94(5):2043–2056

21. Lavernhe S, Quinsat Y, Lartigue C (2010) Model for the prediction of 3D surface topography in 5-axis milling. Int J Adv Manuf Tech 51(9–12):915–924

22. Huang CY, Liang R (2015) Modeling of surface topography in single-point diamond turning machine. Appl Optics 54(23):6979–6985

23. Lin SC, Chang MF (1998) A study on the effects of vibrations on the surface finish using a surface topography simulation model for turning. Int J Mach Tool Manuf 38(7):763–782

24. Omar O, El-Wardany T, Ng E, El-Wardany T, Ng E, Elbestawi MA (2007) An improved cutting force and surface topography prediction model in end milling. Int J Mach Tool Manuf 47(7–8):1263–1275

25. Quinsat Y, Lavernhe S, Lartigue C (2011) Characterization of 3D surface topography in 5-axis milling. Wear 271(3–4):590–595

26. Kelly K, Young P, Byrne G (1999) Modelling the influence of machining dynamics on surface topography in turning. Int J Mech Sci 41(4–5):507–526

27. Gurdal O, Ozturk E, Sims ND (2016) Analysis of process damping in milling. Procedia CIRP 55:152–157